PERGAMON

International Journal of Heat and Mass Transfer 42 (1999) 3405–3418

International Journal of HEAT and MASS TRANSFER

Analysis of cylindrical heat pipes incorporating the effects of liquid–vapor coupling and non-Darcian transport—a closed form solution

N. Zhu[a], K. Vafai[b,*]

[a]Lucent Technologies, Mount Olive, NJ 07828, USA
[b]Department of Mechanical Engineering, The Ohio State University, Columbus, OH 43210, USA

Received 10 June 1998; received in revised form 4 January 1999

Abstract

This paper presents a two-dimensional analytical model for low-temperature cylindrical heat pipes. A closed-form solution which incorporates liquid–vapor interfacial hydrodynamic coupling and non-Darcian transport through the porous wick for the first time, is obtained for predicting the vapor and liquid velocity and pressure distributions. In addition, the steady-state vapor and wall temperatures for a given input heat load in the evaporator region and a convective boundary condition in the condenser region, are obtained. The effects of liquid–vapor interfacial hydrodynamic coupling and non-Darcian transport through the porous wick on the vapor and liquid velocity and pressure distributions as well as the heat pipe capillary limit are discussed and assessed. The analytical solutions of the axial vapor and wall temperature distributions, the vapor and liquid pressure distributions, and the centerline vapor velocities compare very well with both experimental and numerical results. This work constitutes for the first time a comprehensive analytical solution which provides closed form solutions for the vapor and liquid flow as well as the operating temperature and the maximum heat removal capability of the heat pipe. © 1999 Elsevier Science Ltd. All rights reserved.

1. Introduction

Heat pipes are currently used in a wide variety of heat transfer related applications. Analyses of heat pipe operations, both analytical and numerical, have been performed extensively by many investigators. Almost all of the analytical studies have been concentrated on the dynamics of vapor flow. Liquid flow and the liquid–vapor coupling were mostly neglected in analytical studies because of their complexity. A comprehensive analytical model for the overall simulation of steady-state heat pipe operation is not available in open literature. Cao and Faghri [1] investigated the effects of heat pipe wall and the porous wick on the heat pipe operation. They concluded that it is important to include the porous wick and the wall in heat pipe analysis and to treat the entire heat pipe as a single system rather than to analyze the vapor flow alone. Rosenfeld [2] also reported the importance of heat transfer within the wall and the porous wick in the case of an asymmetric heat input.

Due to the difficulty of obtaining an analytical solution for overall heat pipe operation, more and more

* Corresponding author. Tel.: +1-614-292-6560; fax: +1-614-292-3163.
E-mail address: vafai.1@osu.edu (K. Vafai)

0017-9310/99/$ - see front matter © 1999 Elsevier Science Ltd. All rights reserved.
PII: S0017-9310(99)00017-4

Nomenclature

A_1	constant defined in Eq. (44)
A_2	constant defined in Eq. (45)
B	constant defined in Eq. (22)
C	constant defined in Eq. (26)
D	constant defined in Eq. (30)
G_1	constant defined in Eq. (28)
G_2	constant defined in Eq. (34)
h	convective heat transfer coefficient, [W/m^2 K]
h_{fg}	latent heat of working fluid [kJ/kg]
K	permeability of the wick [m^2]
k_{eff}	effective thermal conductivity of the liquid-saturated wick [W/m K]
k_{wall}	thermal conductivity of the heat pipe wall [W/m K]
L	length of heat pipe [m]
L_a	length of the adiabatic section [m]
L_c	length of the condenser section [m]
L_e	length of the evaporator section [m]
M_1	constant defined in Eq. (29)
M_2	constant defined in Eq. (35)
p	pressure [Pa]
p_c	capillary pressure [Pa]
Q	input heat [W]
r	radial coordinate [m]
r_c	effective pore radius of the wick [m]
R_o	heat pipe wall outer radius [m]
R_v	vapor core radius [m]
R_w	heat pipe wall inner radius [m]
Re	injection Reynolds number ($\rho_v v_1 R_v/\mu_v$)
T	temperature [K]
T_b	bulk temperature of the coolant in cooling jack [K]
u	axial velocity [m/s]
u_i	axial interfacial velocity [m/s]
U_v	mean axial vapor velocity [m/s]
U_l	maximum axial liquid velocity [m/s]
v	radial velocity [m/s]
v_1	vapor injection velocity [m/s]
v_2	vapor suction velocity [m/s]
x	axial coordinate [m].

Greek symbols

ϵ	porosity of the wick
γ	porous wick shape parameter ($\sqrt{\epsilon/K}$)
μ	dynamic viscosity [N s/m^2]
ρ	density [kg/m^3]
σ_l	surface tension of the working liquid [N/m].

Subscripts

i	liquid–vapor interface
l	liquid phase
v	vapor phase.

Superscript

+	dimensionless quantity.

numerical models have been developed. Some comprehensive numerical models [3–5] cover both the vapor flow and the liquid flow. The boundary and inertial effects were included in these numerical models by applying the generalized momentum equation in porous medium to describe the liquid flow in heat pipes. The coupling of the liquid and vapor momentum equations was also incorporated in these models by applying either the Laplace–Young equation [3,4] or the momentum jump condition [5] at the liquid–vapor interface. In these models, the matching conditions of velocity and shear stress at the liquid–vapor interface were neglected by assuming a non-slip condition and neglecting the interfacial drag. The effects of these matching conditions as well as the boundary and inertial effects on heat pipe operation have not been investigated in any of the previous studies.

Vafai et al. [6–12] have developed comprehensive pseudo-three-dimensional analytical models for asymmetrical flat-shaped, including both disk-shaped and flat-plate, heat pipes. They incorporated liquid flow, secondary vapor flow and the effects of liquid–vapor hydrodynamic coupling and non-Darcian transport in their models [8–11]. Their results show that, for the flat-shaped heat pipes, while the effects of liquid–vapor interfacial hydrodynamic coupling are negligible, neglecting the boundary and inertial effects can lead to significant error in predicting liquid flow and the maximum heat transfer capability of the heat pipe.

In the present work, a two-dimensional analytical model is developed for the overall simulation of the steady-state cylindrical heat pipe operation. This analytical model employs matched asymptotic expansions for the liquid flow to incorporate liquid–vapor interfacial hydrodynamic coupling and the boundary and inertial effects. A closed-form solution is then obtained based on an in-depth integral method. The effects of liquid–vapor hydrodynamic coupling and the boundary and inertial effects on cylindrical heat pipe operation and operating limit are also investigated. The analytical prediction of vapor and liquid velocity and pressure distribution as well as vapor and wall temperature distributions compare very well with both the experimental data reported by Huang et al. [13] and the numerical results reported by Tournier and El-Genk [5].

2. Mathematical modeling

The schematic of the cylindrical heat pipe and the coordinate system used in the present analysis is shown in Fig. 1. Heat applied at the evaporator section causes vaporization and subsequent pressurization of the working liquid. The vapor flows to the condenser section and releases latent heat as it condenses. The heat is then removed from the condenser wall surface by convection. In the present analysis, vapor and

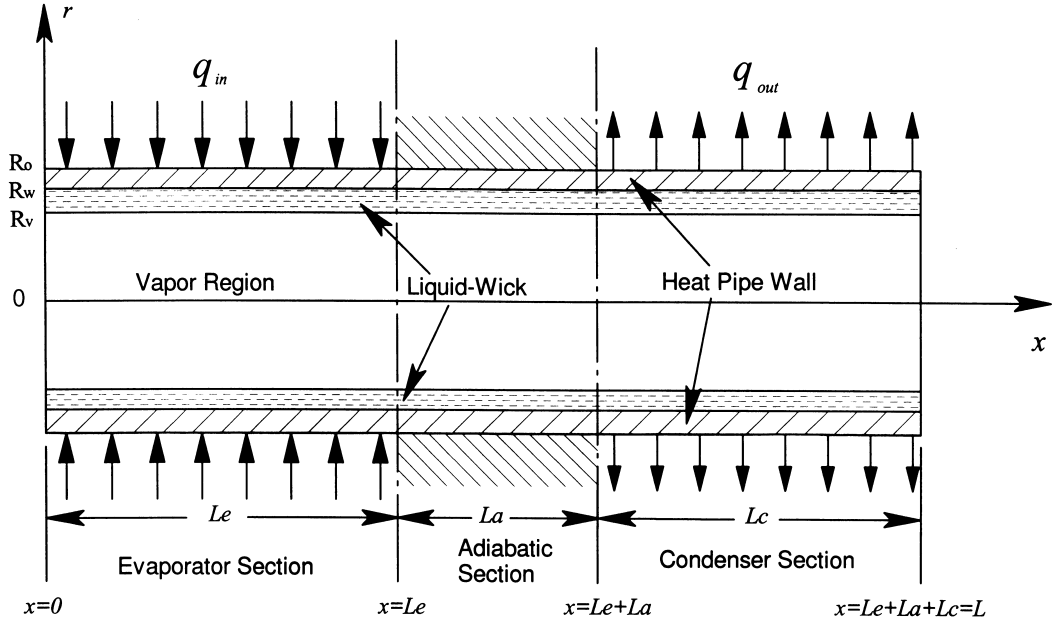

Fig. 1. Schematic of the heat pipe and the coordinate system used in the analysis.

liquid flows are assumed to be steady, laminar and incompressible. The wick is assumed isotropic and saturated with the working liquid. The liquid and vapor phases are coupled at the liquid–vapor interface. The vapor injection and suction at the liquid–vapor interface are assumed to be uniform.

2.1. Governing equations for vapor flow

Based on the above assumptions, the continuity and the momentum equations governing the vapor flow are given by

$$\frac{\partial u_v}{\partial x}+\frac{\partial v_v}{\partial r}+\frac{v_v}{r}=0 \tag{1}$$

$$\rho_v\left(u_v\frac{\partial u_v}{\partial x}+v_v\frac{\partial u_v}{\partial r}\right)=-\frac{\partial p_v}{\partial x}+\mu_v\left(\frac{\partial^2 u_v}{\partial r^2}+\frac{1}{r}\frac{\partial u_v}{\partial r}\right) \tag{2}$$

$$\frac{\partial p_v}{\partial r}=0 \tag{3}$$

The x-direction shear stress in the momentum equations is neglected based on the work of Busse and Prenger [14] which shows the validity of the boundary layer approximation for the vapor flow in long cylindrical heat pipes.

2.2. Governing equations for liquid flow

The liquid flow within the porous wick is modeled using the generalized momentum equation [15] which accounts for the boundary and inertial effects. The convective term in the generalized momentum equation is dropped in accordance with the analysis given in Vafai and Tien [15]. The governing equations for the liquid flow are

$$\frac{\partial u_l}{\partial x}+\frac{1}{r}\frac{\partial}{\partial r}(ru_l)=0 \tag{4}$$

$$\frac{\mu_l}{\epsilon}\left(\frac{\partial^2 u_l}{\partial r^2}+\frac{1}{r}\frac{\partial u_l}{\partial r}\right)-\frac{\mu_l}{K}u_l-\frac{\rho_l F\epsilon}{K^{1/2}}\mid u_l\mid u_l-\frac{\partial p_l}{\partial x}=0 \tag{5}$$

In the above governing equations, ρ_v is the vapor density and ρ_l the liquid density, μ_v the vapor dynamic viscosity, μ_l the liquid dynamic viscosity, K and ϵ are the permeability and porosity of the wick and F is a geometric function based on the porous wick structure and is calculated using the expression outlined in Vafai [16], i.e., $F=1.75/\sqrt{150}\epsilon^{3/2}$.

2.3. Vapor–liquid hydrodynamic coupling

The vapor and liquid phases are coupled at the vapor–liquid interface. The continuity of mass fluxes in the r-direction at the liquid–vapor interface yields

$$\rho_v v_v(x, r=R_v)=\rho_l v_l(x, r=R_v)=\begin{cases}-\rho_v v_1, & 0\le x\le L_e\\ 0, & L_e\le x\le L_e+L_a\\ \rho_v v_2, & L_e+L_a\le x\le L\end{cases} \tag{6}$$

The continuity of axial velocity and shear stresses at the liquid–vapor interface yields

$$u_v(x, r=R_v)=u_l(x, r=R_v)=u_i(x) \tag{7}$$

and

$$\mu_v\frac{\partial u_v}{\partial r}\bigg|_{r=R_v}=\mu_l\frac{\partial u_l}{\partial r}\bigg|_{r=R_v} \tag{8}$$

where $u_i(x)$ is the interfacial velocity at the liquid–vapor interface. The vapor injection velocity, v_1 is related to the input power Q by the following relation:

$$v_1=\frac{Q}{2\rho_v\pi R_v L_e h_{fg}} \tag{9}$$

where h_{fg} is the latent heat of the working fluid. The vapor suction velocity v_2 is determined by the mass balance which requires that the fluid entering the vapor region in the evaporator section to flow out through the condenser section.

2.4. Boundary conditions

The boundary conditions are as follows:

$$x=0:\quad u_v=v_v=u_l=v_l=0 \tag{10}$$

$$x=L:\quad u_v=v_v=u_l=v_l=0,\quad p_v=p_l \tag{11}$$

$$r=0:\quad v_v=0,\quad \frac{\partial u_v}{\partial r}=\frac{\partial p_v}{\partial r}=0 \tag{12}$$

$$r=R_w:\quad u_l=v_l=0 \tag{13}$$

The above governing equations, coupling equations and boundary conditions are used to obtain a closed-form analytical solution for the vapor and liquid velocity and pressure distributions which accounts for the effects of liquid–vapor coupling and non-Darcian transport through the porous wick.

3. Analytical solution

An in-depth integral analysis along with the method of matched asymptotic expansions is employed to obtain the closed-form analytical solution for the vapor and liquid velocity and pressure distributions. The temperature values are then obtained through the use of a simple conduction model.

3.1. Vapor velocity profile

The following velocity profile is utilized for the vapor flow within the heat pipe:

$$u_v(x, r) = U_v(x)(a_0 + a_1 r + a_2 r^2) \tag{14}$$

where

$$U_v(x) = \frac{1}{\pi R_v^2}\int_0^{R_v} u_v(x, r) 2\pi r \, dr \tag{15}$$

is the mean vapor velocity. Applying the boundary conditions given by Eqs. (7) and (12) to Eq. (14) yields the following vapor velocity profile:

$$u_v(x, r) = u_i(x) + 2[U_v(x) - u_i(x)]\left[1 - \left(\frac{r}{R_v}\right)^2\right] \tag{16}$$

3.2. Liquid velocity profile

Vafai and Thiyagaraja [17] have shown that the momentum boundary layer thickness at the interface between a porous medium and a fluid or an impermeable medium is of the order of $(K/\epsilon)^{1/2}$. Utilizing the method of matched asymptotic expansions the liquid velocity profile within the wick region is derived in three parts: an inner solution for the interface zone between the liquid-wick and the vapor phase, an outer solution for the main wick region and an inner solution for the interface zone between the liquid-wick and the heat pipe wall. This results in the following velocity profile:

$$u_l(x, r) = \begin{cases} c_1 + c_2 \exp\left[-\dfrac{r - R_v}{\sqrt{K/\epsilon}}\right] & 0 \le \dfrac{r - R_v}{\sqrt{K/\epsilon}} \le \infty \\ U_l(x) & \text{outer solution} \\ c_3 + c_4 \exp\left[\dfrac{r - R_w}{\sqrt{K/\epsilon}}\right] & -\infty \le \dfrac{r - R_w}{\sqrt{K/\epsilon}} \le 0 \end{cases} \tag{17}$$

where $U_l(x)$ is the maximum liquid velocity. Applying the boundary conditions given by Eqs. (7) and (13) and matching the inner and outer solutions yields

$$u_l(x,r) = \begin{cases} U_l(x) + [u_i(x) - U_l(x)] \exp\left[-\dfrac{r - R_v}{\sqrt{K/\epsilon}}\right] & 0 \le \dfrac{r - R_v}{\sqrt{K/\epsilon}} \le \infty \\ U_l(x) & \text{outer solution} \\ U_l(x) \exp\left[\dfrac{r - R_w}{\sqrt{K/\epsilon}}\right] & -\infty \le \dfrac{r - R_w}{\sqrt{K/\epsilon}} \le 0 \end{cases} \tag{18}$$

Eq. (18) can be written in a more compact form, by utilizing the fact that the thickness of the interface regions, $\sqrt{K/\epsilon}$, is much smaller than $(R_w - R_v)/2$. This results in

$$u_l(x,r) = \begin{cases} U_l(x) + [u_i(x) - U_l(x)] \exp\left[-\dfrac{r - R_v}{\sqrt{K/\epsilon}}\right] & R_v \le r \le \dfrac{R_w + R_v}{2} \\ U_l(x) \exp\left[\dfrac{r - R_w}{\sqrt{K/\epsilon}}\right] & \dfrac{R_w + R_v}{2} \le r \le R_w \end{cases} \tag{19}$$

3.3. The mean vapor velocity

The mean vapor velocity $U_v(x)$ is determined by integrating the vapor continuity equation. Utilizing the vapor velocity profile and the boundary conditions given by Eqs. (6)–(8), (10) and (11), the integration of the vapor continuity Eq. (1) with respect to r from 0 to R_v yields

$$U_v(x) = \begin{cases} \dfrac{2v_1}{R_v} x, & 0 \le x \le L_e \\ \dfrac{2v_1}{R_v} L_e, & L_e \le x \le L_e + L_a \\ \dfrac{2v_2}{R_v}(L - x), & L_e + L_a \le x \le L \end{cases} \tag{20}$$

3.4. The maximum liquid velocity

The maximum liquid velocity $U_l(x)$ is determined by integrating the liquid continuity Eq. (4) with respect to r from R_v to R_w. Applying the liquid velocity profile given by Eq. (19), the mean vapor velocity given by Eq. (20), and the boundary conditions given by Eqs. (6)–(8), (10) and (13) within the integrated liquid continuity equation yields

$$U_l(x) = \begin{cases} -Bv_1 x, & 0 \le x \le L_e \\ -Bv_1 L_e, & L_e \le x \le L_e + L_a \\ -Bv_2(L-x), & L_e + L_a \le x \le L \end{cases} \tag{21}$$

where

$$B = \frac{2R_v}{\rho^+(R_w^2 - R_v^2)}\left(1 + \frac{8\rho^+}{\mu^+\gamma^2 R_v^2}\right) \tag{22}$$

where $\gamma = \sqrt{\epsilon/K}$ is the shape parameter of the porous wick, and $\rho^+ = \rho_l/\rho_v$, $\mu^+ = \mu_l/\mu_v$. If the hydrodynamic coupling is neglected at the liquid–vapor interface, the following expression is obtained for B based on a no-slip condition at the liquid–vapor interface:

$$B = \frac{2R_v}{\rho^+(R_w^2 - R_v^2)} \tag{23}$$

3.5. Interfacial velocity

The interfacial velocity is determined by utilizing the vapor and liquid velocity profiles in Eq. (8). This yields

$$u_i(x) = U_l(x) + \frac{4}{\mu^+\gamma R_v} U_v(x) \tag{24}$$

The fact that $1/\gamma = \sqrt{K/\epsilon} \ll (R_w - R_v)/2$ is used in the derivation of Eq. (24). Substituting Eqs. (20) and (21) into Eq. (24) results in the following expression for u_i(x):

$$u_i(x) = \begin{cases} Cv_1 x, & 0 \le x \le L_e \\ Cv_1 L_e, & L_e \le x \le L_e + L_a \\ Cv_2(L-x), & L_e + L_a \le x \le L \end{cases} \tag{25}$$

where

$$C = \frac{8}{\mu^+\gamma R_v^2} - B \tag{26}$$

Neglecting the hydrodynamic coupling at the liquid–vapor interface leads to $C = 0$.

3.6. Vapor pressure distribution

The pressure distribution in the vapor phase is obtained by integrating the vapor momentum equations with respect to r from 0 to R_v. Introducing vapor continuity equation, vapor velocity profile, vapor-liquid coupling conditions and the related boundary conditions into the integrated momentum equations results in the following derived expression for vapor pressure distribution:

$$p_v(x) = p_v(0) + \begin{cases} (G_1 v_1^2 + M_1 v_1)x^2, & 0 \le x \le L_e \\ (G_1 v_1^2 - M_1 v_1)L_e^2 + 2M_1 v_1 L_e x, & L_e \le x \le L_e + L_a \\ (G_1 v_2^2 - M_1 v_2)(x-L)^2 + M_1 v_2(L + L_a)L_c, & L_e + L_a \le x \le L \end{cases} \tag{27}$$

where

$$G_1 = -\frac{r_v}{3R_v^2}(D^2 - 7D + 16) \tag{28}$$

$$M_1 = -\frac{4\mu_v}{R_v^3}(D - 2) \tag{29}$$

$$D = CR_v \tag{30}$$

If the hydrodynamic coupling at the liquid–vapor interface is neglected, Eq. (27) reduces to

$$p_v(x) = p_v(0) + \begin{cases} \left(-\frac{16\rho_v}{3R_v^2}v_1^2 - \frac{8\mu_v}{R_v^3}v_1\right)x^2, & 0 \le x \le L_e \\ \left(-\frac{16\rho_v}{3R_v^2}v_1^2 + \frac{8\mu_v}{R_v^3}v_1\right)L_e^2 - \frac{16\mu_v}{R_v^3}v_1 L_e x, & L_e \le x \le L_e + L_a \\ \left(-\frac{16\rho_v}{3R_v^2}v_2^2 + \frac{8\mu_v}{R_v^3}v_2\right)(x-L)^2 - \frac{8\mu_v}{R_v^3}v_2(L + L_a)L_c, & L_e + L_a \le x \le L \end{cases} \tag{31}$$

Eq. (31) is similar to that obtained by Faghri [18], which in turn was in agreement with similar relations developed by Busse [19] earlier. It should be noted that in Ref. [18], in addition to not accounting for the liquid–vapor coupling, the non-Darcian effects and for that matter the liquid flow transport was not taken into account. In fact, Ref. [18] considered only the vapor flow.

3.7. Liquid pressure distribution

The liquid pressure distribution is determined by integrating the generalized momentum Eq. (5) with respect to r from R_v to R_w. Integrating Eq. (5) and utilizing all necessary boundary conditions and the cited relationships results in the derivation of the following expression for the liquid pressure distribution:

$$p_l(x) = p_l(0) + \begin{cases} G_2 v_1 x^2 + M_2 v_1^2 x^3, & 0 \le x \le L_e \\ G_2 v_1 L_e(2x - L_e) + M_2 v_1^2 L_e^2(3x - 2L_e), & L_e \le x \le L_e + L_a \\ -G_2 v_2[(x-L)^2 - (L + L_a)L_c] + M_2 v_2^2[(x-L)^3 + (L + 2L_a)L_c^2], & L_e + L_a \le x \le L \end{cases} \quad (32)$$

where

$$p_l(0) = p_v(L) - G_2 v_2(L + L_a)L_c - M_2 v_2^2(L + 2L_a)L_c^2 \quad (33)$$

and

$$G_2 = \frac{\mu_l B}{2K}\left(1 - \frac{1}{\gamma R_v}\,\frac{2}{1 - R_w/R_v}\right) \quad (34)$$

$$M_2 = \frac{\rho_l F \epsilon}{3K^{1/2}}\left[B^2 - \frac{1}{\gamma R_v}\,\frac{C(C-2B)}{1-(R_w/R_v)^2}\right] \quad (35)$$

If the boundary and inertial effects are neglected, G_2 and M_2 are reduced to the following relationships:

$$G_2 = \frac{\mu_l}{2K}\left(B + \frac{1}{\gamma R_v}\,\frac{2C}{1-(R_w/R_v)^2}\right) \quad (36)$$

$$M_2 = 0 \quad (37)$$

3.8. Vapor and wall temperatures

For a fully-thawed low-temperature heat pipe, the vapor phase can be assumed to be saturated and uniform. Therefore, there is no need to solve the energy equation for the vapor phase. The validity of this approximation was examined by Huang and El-Genk [20] experimentally. They measured the axial vapor and wall temperature distributions of a copper heat pipe with water as the working fluid. Their results show that the vapor temperature is uniform along the heat pipe. They also found that the wall temperature in the evaporator and the condenser sections is almost uniform, except near the interfaces with the adiabatic section where axial conduction in the wall is most pronounced. In the present study, the heat pipe is heated uniformly over the evaporator section and convectively cooled in the condenser section. The vapor temperature is assumed uniform along the heat pipe, and a one-dimensional heat conduction model is used for the wall and liquid-wick regions. For steady-state operation, the convective boundary condition at the wall outer surface ($r = R_o$) is:

$$Q = 2\pi R_o L_c h(T_{wall,c} - T_b) \quad (38)$$

where Q is the heat input, h is the convective heat transfer coefficient, $T_{wall,c}$ is the wall temperature in the condenser section, and T_b is the bulk temperature of the coolant. The vapor and wall temperatures are obtained as follows:

$$T_v = T_b + \frac{Q}{2\pi L_c}\left(\frac{\ln(R_o/R_w)}{k_{wall}} + \frac{\ln(R_w/R_v)}{k_{eff}} + \frac{1}{hR_o}\right) \quad (39)$$

and

$$T_{wall}(x) = \begin{cases} T_b + \dfrac{Q}{2\pi L_c}\left[\left(\dfrac{\ln(R_o/R_w)}{k_{wall}} + \dfrac{\ln(R_w/R_v)}{k_{eff}}\right)\left(1 + \dfrac{L_c}{L_e}\right) + \dfrac{1}{hR_o}\right] & 0 \le x \le L_e \\ T_b + \dfrac{Q}{2\pi L_c}\left(\dfrac{\ln(R_o/R_w)}{k_{wall}} + \dfrac{\ln(R_w/R_v)}{k_{eff}} + \dfrac{1}{hR_o}\right) & L_e \le x \le L_e + L_a \\ T_b + \dfrac{Q}{2\pi h R_o L_c} & L_e + L_a \le x \le L \end{cases} \quad (40)$$

where k_{wall} is the thermal conductivity of the heat pipe wall, and k_{eff} is the effective thermal conductivity of the liquid-saturated wick.

3.9. The maximum heat transport capillary limit

For a heat pipe under steady-state operation, stable circulation of the working fluid in the heat pipe is achieved through the capillary pressure established by the wick structure. In conventional heat pipes, there exists a maximum capillary pressure that can be developed for a liquid–vapor pair. The maximum heat transport capillary limit for a heat pipe is achieved when the sum of the pressure losses along the circulation path of the working fluid reaches the maximum capillary pressure; that is

$$\Delta p_v(x_{max} - x_{min}) + \Delta p_l(x_{min} - x_{max}) + p_c(x_{min}) = \frac{2\sigma_l}{r_c} \quad (41)$$

where $p_c(x_{min}) = p_v(x_{min}) - p_l(x_{min})$ is the minimum capillary pressure, σ_l is the surface tension of the liquid, r_c is the effective pore radius of the wick, and x_{max}/x_{min} denotes the location where the capillary pressure is maximum/minimum. The notation $\Delta p(x_{max} - x_{min})$ refers to evaluation of Δp over the distance $(x_{max} - x_{min})$. In the present study, as stated in Eq. (11) the condenser end $(x = L)$ is assumed to be the wet point $(p_v(L) = p_l(L))$ during steady-state operation. This reduces Eq. (41) to

$$p_v(0) - p_l(0) = \frac{2\sigma_l}{r_c} \quad (42)$$

Substituting Eqs. (9), (31) and (33) into Eq. (42) and solving for the maximum heat transport capillary limit yields

$$Q_{max} = \frac{1}{2A_1}\left(\sqrt{A_2^2 + 8A_1\sigma_l/r_c} - A_2\right) \quad (43)$$

where Q_{max} is the maximum heat transport capillary limit, and

$$A_1 = \frac{M_2(L + 2L_a)}{12\pi^2 R_v^2 \rho_v^2 h_{fg}^2} \quad (44)$$

$$A_2 = \frac{(G_2 - 2M_1)(L + L_a)}{4\pi R_v \rho_v h_{fg}} \quad (45)$$

When boundary and inertial effects are neglected, Eq. (43) reduces to

$$Q_{max} = \frac{2\sigma_l}{A_2 r_c} \quad (46)$$

4. Results and discussion

To verify the model predictions, results are compared with the experimental data reported by Huang et al. [13] and the numerical results reported by Tournier and El-Genk [5], for a copper heat pipe with water as the working fluid. The physical dimensions of the heat pipe are chosen as: $R_o = 9.55$ mm, $R_w = 9.4$ mm, $R_v = 8.65$, $L_e = 60$ cm, $L_a = 9$ cm, and $L_c = 20$ cm which are based on the physical dimensions used in Refs. [5] and [13]. The wick effective pore radius, porosity and permeability are chosen as 54 μm, 0.9 and 1.5×10^{-9} m^2, respectively. The effective thermal conductivity of the liquid-wick is calculated to be 1.965 W/m K, using the equation given by Chi [21]. The thermophysical properties of the working fluid are obtained at the calculated vapor temperature and are assumed to be constant along the heat pipe. The input heat is taken as 455 W. The cooling water enters the condenser cooling jacket at 294.5 K and 11.33 g/s. The temperature of the cooling water at the exit of the cooling jacket is calculated using the equation $Q = \dot{m}c_p(T_{out} - T_{in})$. The bulk temperature of the cooling water is taken as the arithmetic mean of T_{in} and T_{out}. The convective heat transfer coefficient in the cooling jacket is taken as 1800 W/m^2 K [5]. It should be noted that a great advantage of the presented closed form analytical solution is the ease and speed in which a comprehensive solution can be obtained subject to changes in various parameter and properties. In here some representative values were chosen for the simulations. We were able to show that the main conclusions remain unchanged for wide range of variation of these parameters.

Fig. 2 compares the model predictions with the numerical and experimental results of the vapor and wall temperature distributions along the heat pipe. The model predictions of both the vapor and the wall temperatures agree well with the numerical and the experimental values. As can be seen in Fig. 1, the assumption of uniform vapor temperature along the heat pipe is good for low-temperature heat pipes. Although there is a discrepancy between the calculated wall temperature and the experimental data at the beginning and the end of the condenser section, the model predictions agree very well with the numerical results reported by Tournier and El-Genk [5]. Since same parameter values for the convective cooling boundary condition are used in the present analytical model as those used in the numerical model, the good agreement between the analytical and the numerical results of the wall temperatures demonstrates that the one-dimensional approximation for the heat transfer within the wall and liquid-wick regions is adequate for low-temperature heat pipes. This is in agreement with the observation of Tournier et al. [22].

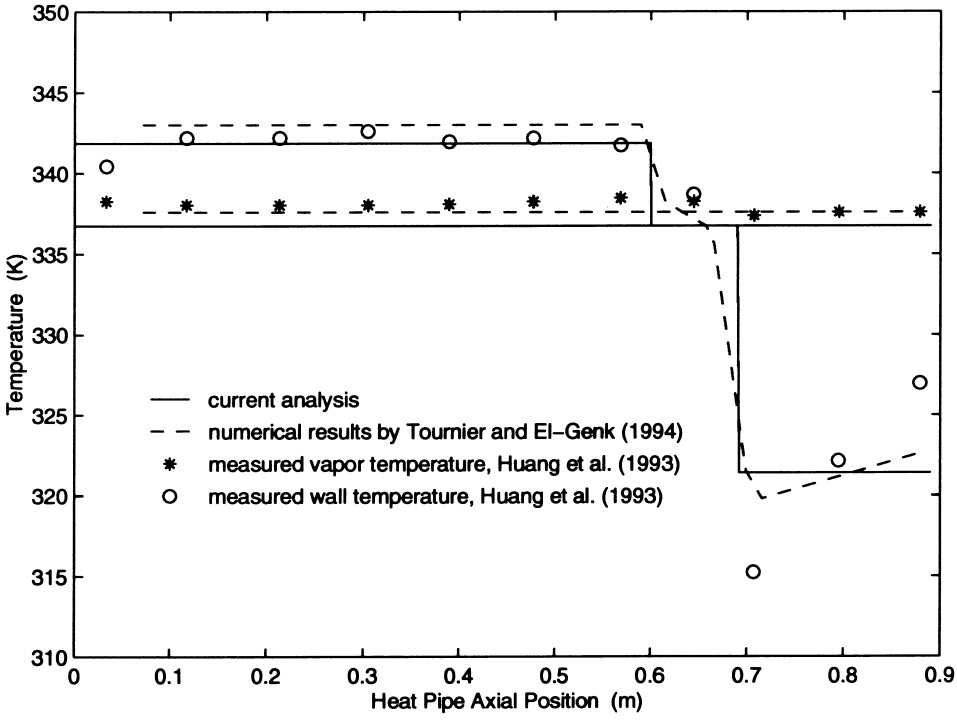

Fig. 2. Comparison of the calculated vapor and wall temperature distributions with the numerical results given by Tournier and El-Genk [5] and the experimental results given by Huang et al. [13].

Fig. 3 compares the analytical vapor and liquid pressure distributions along the heat pipe with the numerical results of Tournier and El-Genk [5]. The absolute value of the vapor pressure at the evaporator end, $p_v(0)$, is related to the calculated vapor temperature based on the assumption that the vapor phase is saturated for a low-temperature fully-thawed heat pipe. The analytical results agree very well with the numerical results. As the results show, the vapor pressure variation along the heat pipe is small, which means that a uniform vapor temperature profile is expected.

The variations of the mean vapor velocity, the centerline vapor velocity, the maximum liquid velocity and the interfacial velocity along the heat pipe are shown in Figs. 4 and 5. The positive velocity value denotes that the flow is along the x direction and the negative velocity value denotes that the flow is along the negative x direction. The analytical centerline vapor velocity at the exit of the evaporator is compared to the numerical result by Tournier and El-Genk [5]. Again, as seen in Fig. 4, the analytical predictions agree very well with the numerical results. This further demonstrates that the analytical model provides accurate predictions of the low-temperature heat pipe operations.

The effects of liquid–vapor interfacial hydrodynamic coupling and the boundary and inertial effects are analyzed next. Results were obtained for the radial Reynolds number ($Re = \rho_v v_1 R_v/\mu_v$) values of 2.0, 5.0 and 10.0 and are displayed in Figs. 6–8. To accommodate vapor and liquid pressures at different Re values in the same figure and to make the comparison more meaningful, the vapor pressure at the evaporator end, $p_v(0)$, is taken as zero in Figs. 7 and 8 for all the Re values. The effects of liquid–vapor interfacial hydrodynamic coupling on the maximum liquid velocity along the heat pipe is shown in Fig. 6. It should be mentioned that liquid–vapor interfacial hydrodynamic coupling has no effect on the mean vapor velocity, as indicated in Eq. (20). This is because the vapor flow rate at steady-state operation is purely determined by the vapor injection/suction velocities, i.e., the evaporation/condensation rates. However, liquid–vapor interfacial hydrodynamic coupling do affect the vapor velocity profile, as illustrated in Eq. (16). For example, the interfacial effects result in a larger centerline vapor velocity. Since the interfacial velocity is negligible compared to the mean vapor velocity, as can be seen in Figs. 4 and 5, the interfacial effects on the vapor velocity profile is negligible. The analytical results in Fig.

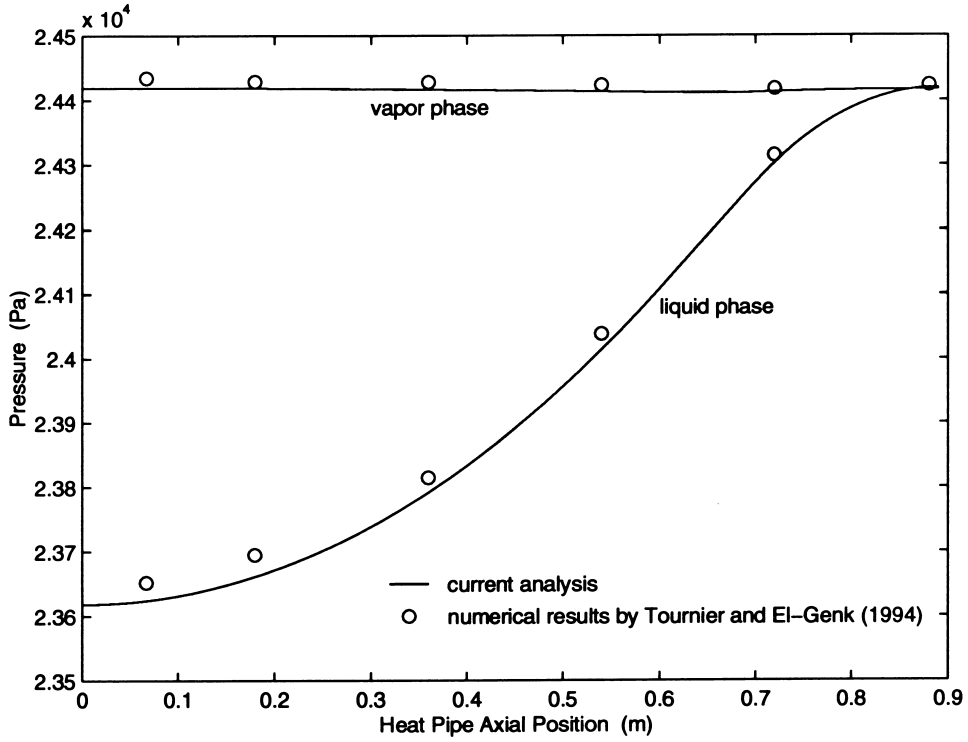

Fig. 3. Comparison of the calculated vapor and liquid pressure distributions with the numerical results given by Tournier and El-Genk [5].

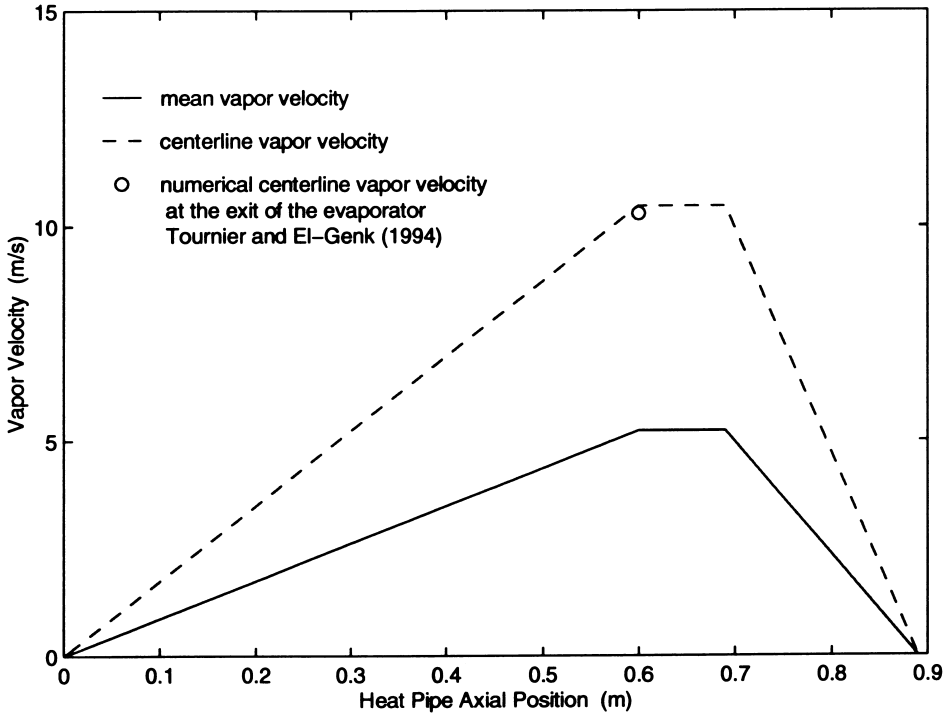

Fig. 4. Variations of the mean vapor velocity and the centerline vapor velocity along the heat pipe.

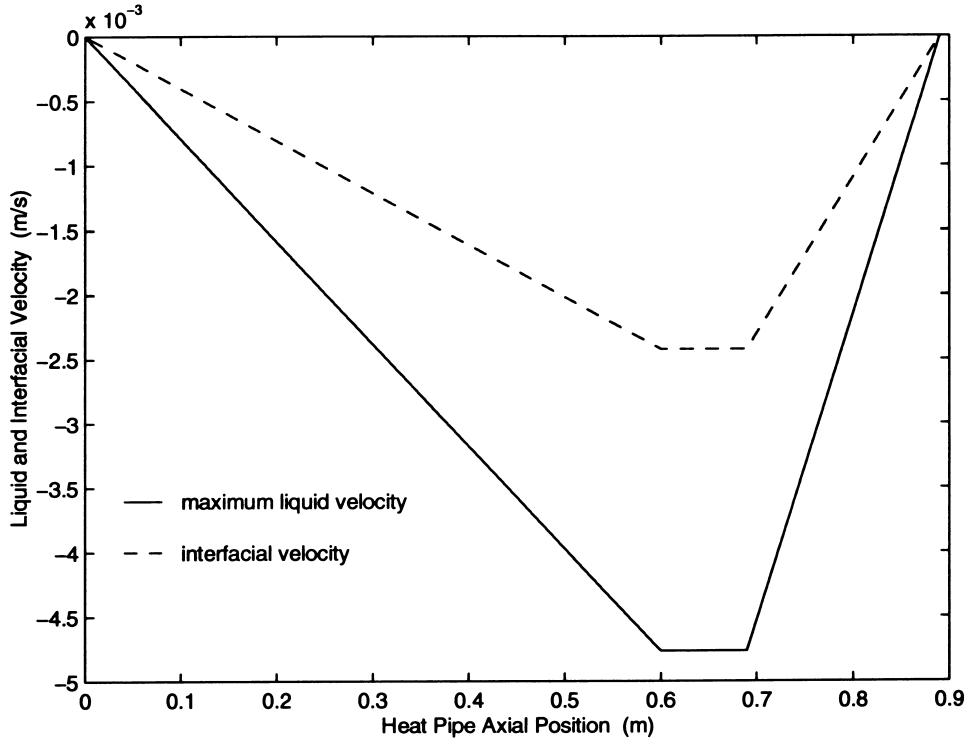

Fig. 5. Variations of maximum liquid velocity and interfacial velocity along the heat pipe.

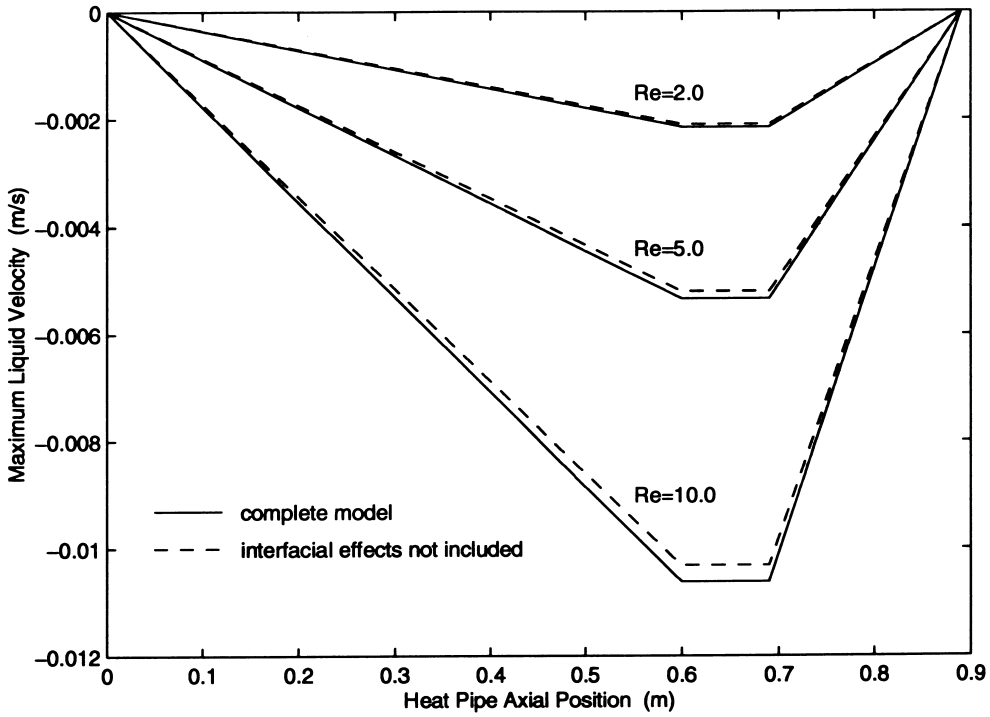

Fig. 6. The effects of liquid–vapor interfacial hydrodynamic coupling on the maximum liquid velocities.

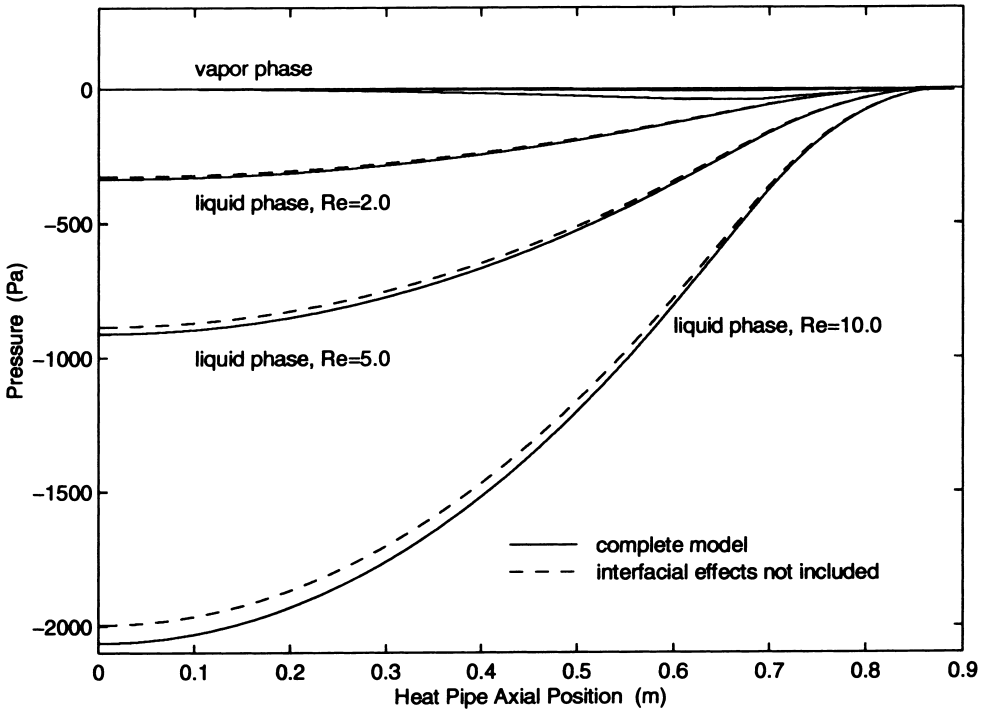

Fig. 7. The effects of liquid–vapor interfacial hydrodynamic coupling on vapor and liquid pressures.

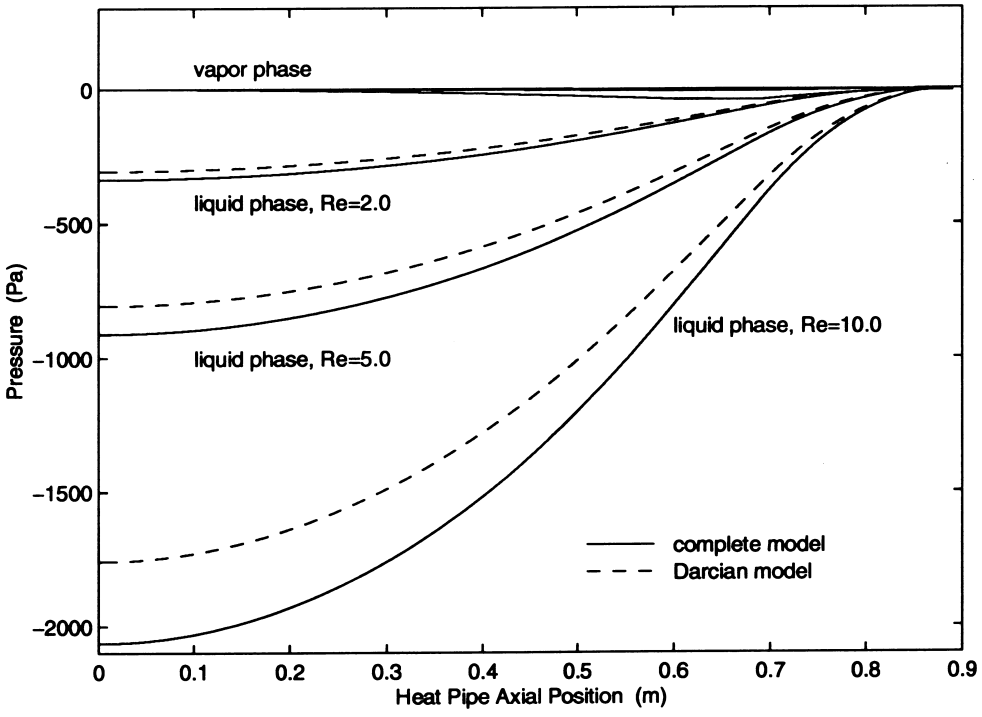

Fig. 8. Boundary and inertial effects on the vapor and liquid pressure distributions.

6 show that the interfacial effects lead to a larger maximum liquid velocity. The larger the injection Reynolds number, the larger the difference caused by the interfacial effects. Fig. 7 shows the effects of liquid–vapor interfacial hydrodynamic coupling on the vapor and liquid pressures. The interfacial effect on the vapor pressure is negligible. However, neglecting liquid–vapor interfacial hydrodynamic coupling will lead to a smaller liquid pressure drop along the heat pipe.

The boundary and inertial effects on vapor and liquid pressure profiles are shown in Fig. 8. As indicated in Eq. (27), the pressure distribution in the vapor phase is not affected by the boundary and inertial effects. However, neglecting the boundary and inertial effects leads to an underestimation of the liquid pressure. The larger the Reynolds number, the larger the error involved in the calculation of liquid pressures by using a Darcian model. This is in agreement with the results by Vafai and Tien [15].

Fig. 9 shows the interfacial and the boundary and inertial effects on the heat transport capillary limit of the heat pipe. It can be seen in Fig. 9 that either neglecting the interfacial effects or neglecting the boundary and inertial effects can lead to an overestimation of the capillary limit. This is because a smaller overall liquid pressure drop along the heat pipe is expected when the interfacial effects or the boundary and inertial effects are neglected. While the interfacial effects on the maximum heat removal capability is relatively small, the error involved in neglecting the boundary and inertial effects is substantial.

5. Conclusions

The steady-state operation of a low-temperature cylindrical heat pipe has been studied analytically. An analytical model, which incorporates liquid–vapor interfacial hydrodynamic coupling and non-Darcian transport through the porous wick, was developed for predicting the vapor and liquid flow and the maximum heat transfer capability of the heat pipe. A closed-form solution was obtained for the vapor and wall temperatures as well as the vapor and liquid velocity and pressure distributions for a convective cooling condition in the condenser region. A closed-form solution of the heat pipe capillary limit during steady state operation was also obtained. These closed-form analytical solutions, provide a quick, accurate prediction method for low-temperature heat pipe operation and were found to be in very good agreement with both experimental and numerical results. The effects of liquid–

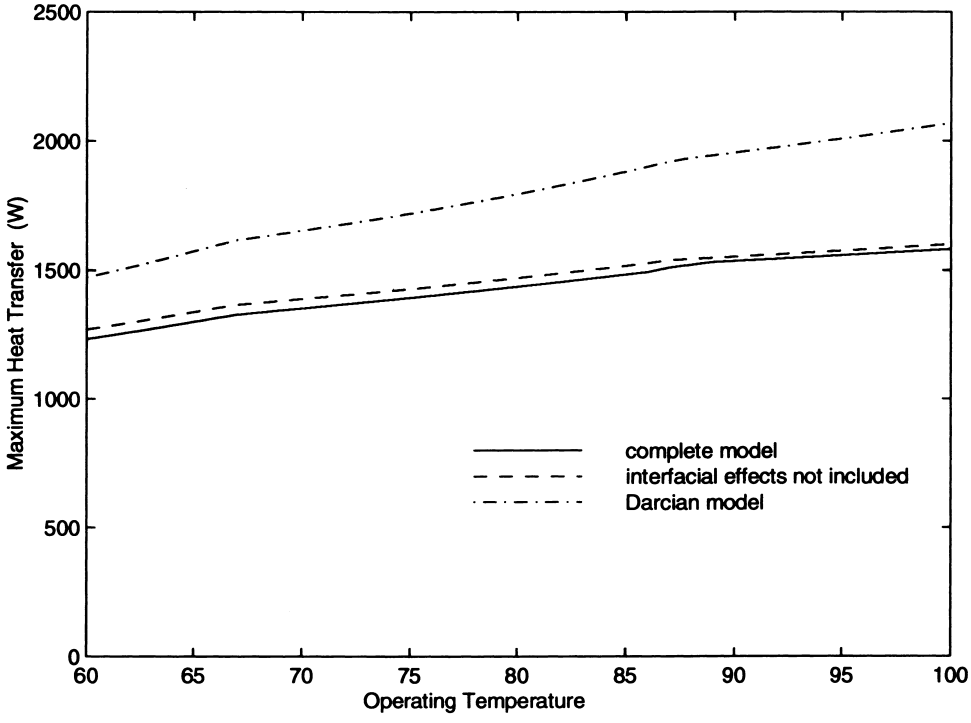

Fig. 9. The effects of liquid–vapor interfacial hydrodynamic coupling and the boundary and inertial effects on the heat pipe capillary limit.

vapor interfacial hydrodynamic coupling and non-Darcian transport through the porous wick were also analyzed. The results show that the interfacial effects are small and can be neglected. However, substantial errors can occur when using Darcy's law in calculating the liquid pressure distributions as well as the maximum heat removal capability of the heat pipe.

Acknowledgement

The grant (DE-F602-93ER61612) by the Department of Energy is acknowledged and greatly appreciated.

References

[1] Y. Cao, A. Faghri, Transient two-dimensional compressible analysis for high temperature heat pipes with pulsed heat input, Numerical Heat Transfer 114 (1990) 1028–1035.

[2] J.H. Rosenfeld, Modeling of heat transfer into a heat pipe for a localized heat input zone, in: AIChE Symposium Series, no. 257, vol. 83, 1987, pp. 71–76.

[3] V.H. Ransome, H. Chow, ATHENA heat pipe transient model, in: Trans. 4th Symposium on Space Nuclear Power Systems, CONF-870102-Summs., Albuquerque, NM, 1987, pp. 389–392.

[4] J.M. Doster, M.L. Hall Numerical modeling of high-temperature liquid-metal heat pipes, 1989 Joint ASME/A.I.Ch.E National Heat Transfer Conference, Philadelphia, PA, vol. 89-HT-13, 1989, pp. 1–9.

[5] J.M. Tournier, M.S. El-Genk, A heat pipe transient analysis model, Int. J. Heat Mass Transfer 37 (1994) 753–762.

[6] K. Vafai, W. Wang, Analysis of flow and heat transfer characteristics of an asymmetrical flat plate heat pipe, Int. J. Heat Mass Transfer 35 (1992) 2087–2099.

[7] K. Vafai, N. Zhu, W. Wang, Analysis of assymetrical disk-shaped and flat plate heat pipes, ASME J. Heat Transfer 117 (1995) 209–218.

[8] N. Zhu, K. Vafai, The effects of liquid–vapor coupling and non-Darcian transport on asymmetrical disk-shaped heat pipes, Int. J. Heat Mass Transfer 39 (1996) 2095–2113.

[9] N. Zhu, K. Vafai, Optimization of asymmetrical disk-shaped heat pipes, AIAA J. Thermophys. Heat Transfer 10 (1996) 179–182.

[10] N. Zhu, K. Vafai, Numerical and analytical investigation of vapor flow in a disk-shaped heat pipe incorporating secondary flow, Int. J. Heat Mass Transfer 40 (1997) 2887–2900.

[11] N. Zhu, K. Vafai, Analytical modeling of the startup characteristics of asymmetrical flat-plate and disk-shaped heat pipes, Int. J. Heat Mass Transfer 41 (1998) 2619–2637.

[12] N. Zhu, K. Vafai, Vapor and liquid flow in an asymmetrical flat plate heat pipe: a three-dimensional analytical and numerical investigation, Int. J. Heat Mass Transfer 41 (1998) 159–174.

[13] L. Huang, M.S. El-Genk, J-M. Tournier, Transient performance of an inclined water heat pipe with a screen wick, ASME National Heat Transfer Conference, Atlanta GA, Heat Pipes and Capillary Pumped Loops, HTD-vol. 236, 1993, pp. 87–92.

[14] C.A. Busse, F.C. Prenger, Numerical analysis of the vapor flow in cylindrical heat pipes, in: Proc. 5th Int. Heat Pipe Conf., Part 1, JIATEC, Tokyo, Japan, 1984, pp. 214–219.

[15] K. Vafai, C.L. Tien, Boundary and inertia effects on flow and heat transfer in porous media, Int. J. Heat Mass Transfer 24 (1981) 195–203.

[16] K. Vafai, Convective flow and heat transfer in variable porosity media, J. Fluid Mech 147 (1984) 233–259.

[17] K. Vafai, R. Thiyagaraja, Analysis of flow and heat transfer at the interface region of a porous medium, Int. J. Mass Transfer 30 (1987) 1391–1405.

[18] A. Faghri, Performance characteristics of a concentric annular heat pipe: Part II—vapor flow analysis, ASME J. Heat Transfer 111 (1989) 851–857.

[19] C.A. Busse, Pressure drop in the vapor phase of long heat pipes, in: Proc. Thermionic Conversion Specialist Conference, Palo Alto, CA, 1967, pp. 391–398.

[20] L. Huang, M.S. El-Genk, Experimental investigation of transient operation of a water heat pipe, in: Proceedings of 10th Symposium on Space Nuclear Power and Propulsion, Albuquerque, NM, 1993, pp. 365–374.

[21] S.W. Chi, Heat Pipe Theory and Practice, Hemisphere, Washington, DC, 1976.

[22] J-M. Tournier, M.S. El-Genk, A.J. Juhasz, Heat-pipe transient model for space applications, in: Proceedings of 8th Symposium on Space Nuclear Power Systems, Albuquerque, NM, 1991, pp. 857–868.